JGR Space Physics

RESEARCH ARTICLE
10.1029/2024JA033233

Magnetosheath Plasma Flow and Its Response to IMF and Geodipole Tilt as Obtained From the Data-Based Modeling

N. A. Tsyganenko[1], V. S. Semenov[1], N. V. Erkaev[2,3], and N. T. Gubaidulin[1]

[1]Saint Petersburg State University, Saint Petersburg, Russia, [2]Institute of Computational Modelling of Siberian Branch of the Russian Academy of Sciences, Krasnoyarsk, Russian Federation, [3]Applied Mechanics Cathedra, Siberian Federal University, Krasnoyarsk, Russian Federation

Key Points:

- Large-scale patterns of the magnetosheath plasma flow are reconstructed from multi-year sets of in situ data and an advanced empirical model
- Substantial interplanetary magnetic field influence on the flow patterns is revealed, induced by magnetic field compression and tensions inside the magnetosheath
- Plasma flows significantly depend on the dipole tilt, indicating the important role of reconnection effects around the dayside magnetopause

Correspondence to:
N. A. Tsyganenko,
n.tsyganenko@spbu.ru

Citation:
Tsyganenko, N. A., Semenov, V. S., Erkaev, N. V., & Gubaidulin, N. T. (2024). Magnetosheath plasma flow and its response to IMF and geodipole tilt as obtained from the data-based modeling. *Journal of Geophysical Research: Space Physics*, *129*, e2024JA033233. https://doi.org/10.1029/2024JA033233

Received 27 AUG 2024
Accepted 19 OCT 2024

Author Contributions:
Conceptualization: N. A. Tsyganenko, V. S. Semenov, N. V. Erkaev
Data curation: N. A. Tsyganenko, N. T. Gubaidulin
Formal analysis: N. A. Tsyganenko, N. V. Erkaev
Funding acquisition: V. S. Semenov
Investigation: N. A. Tsyganenko
Methodology: N. A. Tsyganenko, V. S. Semenov
Project administration: V. S. Semenov
Resources: V. S. Semenov
Software: N. A. Tsyganenko
Supervision: V. S. Semenov
Validation: N. A. Tsyganenko
Visualization: N. A. Tsyganenko
Writing – original draft: N. A. Tsyganenko
Writing – review & editing: N. A. Tsyganenko, V. S. Semenov, N. V. Erkaev

Abstract Large-scale patterns of the steady-state magnetosheath plasma flow and their dependence on the interplanetary magnetic field (IMF) have been reconstructed for the first time on the basis of large multi-year multi-mission pool of spacecraft observations, concurrent interplanetary data, and an empirical high-resolution model. The flow model architecture builds upon a recently developed magnetosheath magnetic field representation by flexible expansions of its toroidal and poloidal components in a coordinate system, naturally conformed with the magnetopause and bow shock shapes. The model includes two physics-based flow symmetry modes: the first one treats the magnetosphere as an axisymmetric unmagnetized obstacle, whereas the second mode takes into account the geodipole tilt, an important factor in the reconnection effects. The spacecraft data pool includes 1-min average data by Themis (2007–2024), Cluster (2001–2022), and MMS-1 (2015–2024) missions, as well as OMNI interplanetary data. The model drivers include the solar wind particle flux, IMF components, and the geodipole tilt angle. The model calculations faithfully reproduce the average plasma flow geometry and substantial effects have been found of the IMF orientation and magnitude, a principal factor that defines electromagnetic forces inside the magnetosheath. A strong dependence of the magnetosheath flow patterns on the Earth's dipole tilt indicates an important contribution of reconnection effects at the magnetopause to the solar wind particle transport around the dayside magnetosphere.

Plain Language Summary As a result of the solar wind interaction with the geomagnetic field, the Earth's magnetosphere becomes embedded within a huge “cocoon”, a vast region between the bow shock and the magnetopause, where the incoming plasma stream gets compressed, heated, and diverted sideways around the magnetospheric boundary. An important factor that significantly affects the magnetosheath flow is the interplanetary magnetic field (IMF), transported to the Earth's orbit from the solar corona. The IMF undergoes compression and deformation inside the magnetosheath; the resulting electromagnetic forces substantially affect the plasma flow. Furthermore, the magnetic fields of solar and terrestrial origin can reconnect at the magnetopause, which results in additional modifications of the plasma flow pattern. During the last decades, huge amounts of satellite data were obtained in the near-Earth space; using them in combination with a flexible mathematical model allowed us to quantitatively reconstruct the magnetosheath plasma flows and their dependence on the interplanetary factors and orientation of the Earth's magnetic dipole. The present paper describes first results of that study.

1. Introduction

Notwithstanding the widespread and fast-expanding use of first-principle simulations, the data-constrained modeling remains an effective instrument for studying the geospace and its response to interplanetary conditions. This is especially true in view of the tremendous inflow of new data and rapidly growing historical data archives during the last decades. Since almost two centuries ago, a traditional object of the data-based modeling has been the geomagnetic field, starting from the first main field model developed by Gauss in the late 1830s and followed much later by first successful attempts (Mead & Fairfield, 1975) to expand the modeling region from the ground and low altitudes to the distant magnetosphere. Except for purely statistical studies (e.g., Dimmock et al., 2020; Zhang et al., 2019), relatively less attention was paid to the data-based modeling of the turbulent magnetosheath. First successful efforts in that area were made recently by Michotte de Welle et al. (2022, 2024), who directly reconstructed the magnetosheath magnetic field from a large pool of spacecraft data, making it possible to visualize the field line draping about the magnetosphere. Jung et al. (2024) provided a parameterized magnetosheath model, though based solely on simulations and theory. A different approach, employing an advanced

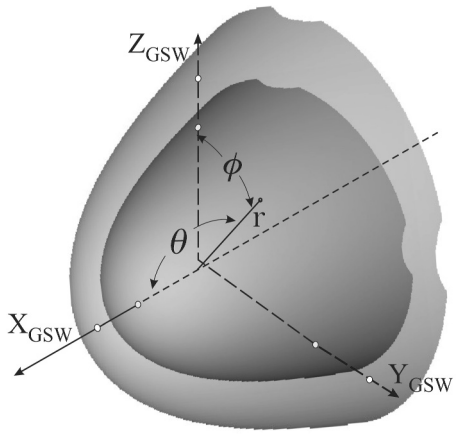

Figure 1. (From TSE23/TSEG24). Illustrating the coordinates. Cartesian: GSW system with X-axis antiparallel to solar wind flow; spherical: radial distance r, cone and clock angles $\theta = \arccos(X/r)$ and $\phi = \arctan(Y/Z)$, resp. The gray-shaded surfaces are those of constant $\delta(r,\theta)$, such that $\delta = 0$ corresponds to the model magnetopause.

mathematical model of the magnetosheath field and a large spacecraft data archive was pursued in two recent studies by Tsyganenko et al. (2023, 2024; referred henceforth as TSE23 and TSEG24), which made it possible to quantitatively represent the magnetic field and electric currents for various IMF orientations by means of self-contained model algorithms.

The next natural and challenging question is, whether it is possible to use the archived data and a similar empirical approach to reconstruct the plasma bulk flows around the magnetosphere and explore their response to IMF orientation and magnitude? Previous efforts in this direction should be mentioned, namely, a study by Soucek and Escoubet (2012) and a more recent work by Narita et al. (2023). Both of them adhered to an earlier developed approach by Kobel and Flückiger (1994), based on a grossly simplified assumption of current-free magnetic field. Moreover, the study by Narita et al. was based on representing the plasma velocity as the gradient of a scalar potential. Given the complex turbulent nature of the observed magnetosheath with strongly compressed/deformed magnetic fields and sheared (hence, rotational) plasma flows, neither of the above assumptions is realistic.

In this paper we present first results of an attempt to empirically model the magnetosheath plasma flow, based on a large pool of in situ plasma and magnetometer data taken during the last decades and a flexible mathematical model, derived along the same lines as the previously developed magnetosheath magnetic field representations. The paper is organized as follows: the next Section 2 describes the model architecture, Section 3 briefly outlines the data base, Section 4 presents main results, the Discussion Section 5 focuses on the dipole tilt effects, and Section 6 summarizes the results.

2. Model

Following the approach of TSE23 and TSEG24, we employ Cartesian GSW system, similar to the standard GSM, but with X axis antiparallel to the observed solar wind flow and Z axis lying in the plane defined by the X axis and the geodipole moment. Thus defined X_{GSW}, Y_{GSW}, and Z_{GSW} are then transformed into the $\{\delta,\theta,\phi\}$ coordinate system, naturally conformed with the observed shape of the magnetopause and bow shock, as shown in Figure 1 (reproduced from our above cited papers). The coordinate

$$\delta(r,\theta) = 1 - r\cos^{2\alpha}(\theta/2)/R_S \tag{1}$$

serves as a measure of separation between an arbitrary point $\{r,\theta,\phi\}$ and the axially symmetric surface $r_S(\theta,R_S,\alpha) = R_S/\cos^{2\alpha}(\theta/2)$, first proposed by Shue et al. (1997) as a simple model approximation for the magnetopause shape and size. Here R_S is the subsolar radius of the boundary, while α quantifies its dayside curvature and tailward expansion rate.

The model architecture is based on representing the bulk particle flow vector $\mathbf{F} = \rho\mathbf{v}$ with a sum of toroidal and poloidal parts

$$\mathbf{F} = \sum_{l,n,m} \nabla\Psi_{\mathrm{t}}^{(lnm)} \times \nabla\delta + \nabla \times \sum_{l,n,m} \nabla\Psi_{\mathrm{p}}^{(lnm)} \times \nabla\delta \tag{2}$$

whose generating functions Ψ_{t} and Ψ_{p} are each expanded into triple sums

$$\Psi_t(r,\theta,\phi) = \sum_{l=0}^{L} \delta^l(r,\theta) \sum_{n=1}^{N} \sum_{m=0}^{n} V_t^{(lnm)}(\theta,\phi) \tag{3}$$

$$\Psi_p(r,\theta,\phi) = \sum_{l=0}^{L} \delta^l(r,\theta) \sum_{n=1}^{N} \sum_{m=0}^{n} V_p^{(lnm)}(\theta,\phi), \tag{4}$$

where $V_t^{(lnm)}$ and $V_p^{(lnm)}$ are standard spherical functions

$$V_t^{(lnm)} = P_n^m(\cos\theta)\left(g_{lnm}^{(t)}\cos m\phi + h_{lnm}^{(t)}\sin m\phi\right) \tag{5}$$

$$V_p^{(lnm)} = P_n^m(\cos\theta)\left(g_{lnm}^{(p)}\cos m\phi + h_{lnm}^{(p)}\sin m\phi\right) \tag{6}$$

with free unknown coefficients $g_{lnm}^{(t)}$, $h_{lnm}^{(t)}$, $g_{lnm}^{(p)}$, and $h_{lnm}^{(p)}$.

Accordingly, the total toroidal and poloidal components of the flow vector read

$$\mathbf{F}_t = \sum_{l=0}^{L}\sum_{n=1}^{N}\sum_{m=0}^{n}\mathbf{f}_t^{(lnm)} \quad \text{and} \quad \mathbf{F}_p = \sum_{l=0}^{L}\sum_{n=1}^{N}\sum_{m=0}^{n}\mathbf{f}_p^{(lnm)}, \tag{7}$$

where the partial flows $\mathbf{f}_t^{(lnm)}$ and $\mathbf{f}_p^{(lnm)}$ implicitly include the coefficients $g_{lnm}^{(t)}$, $h_{lnm}^{(t)}$, $g_{lnm}^{(p)}$, $h_{lnm}^{(p)}$, each of which is expanded into linear combinations of concurrent external drivers: (a) the solar wind proton flux $F_{\rm sw} = n_p v_{\rm sw}$, (b) IMF B_x, B_y, B_z, and (c) sine/cosine of the geodipole tilt angle ψ, such that

$$\begin{aligned} g_{lnm}^{(t,p)} = {} & F_{\rm sw}\left[g_{lnm}^{(t,p,0)} + g_{lnm}^{(t,p,1)}\cos\psi + g_{lnm}^{(t,p,2)}\sin\psi + g_{lnm}^{(t,p,3)}B_x + g_{lnm}^{(t,p,4)}B_y + g_{lnm}^{(t,p,5)}B_z\right. \\ & + g_{lnm}^{(t,p,6)}B_xB_y + g_{lnm}^{(t,p,7)}B_xB_z + g_{lnm}^{(t,p,8)}B_x\sin\psi + g_{lnm}^{(t,p,9)}B_x\cos\psi \\ & \left. + g_{lnm}^{(t,p,10)}B_y\sin\psi + g_{lnm}^{(t,p,11)}B_y\cos\psi + g_{lnm}^{(t,p,12)}B_z\sin\psi\right] \end{aligned} \tag{8}$$

$$\begin{aligned} h_{lnm}^{(t,p)} = {} & F_{\rm sw}\left[h_{lnm}^{(t,p,0)} + h_{lnm}^{(t,p,1)}\cos\psi + h_{lnm}^{(t,p,2)}\sin\psi + h_{lnm}^{(t,p,3)}B_x + h_{lnm}^{(t,p,4)}B_y + h_{lnm}^{(t,p,5)}B_z\right. \\ & + h_{lnm}^{(t,p,6)}B_xB_y + h_{lnm}^{(t,p,7)}B_xB_z + h_{lnm}^{(t,p,8)}B_x\sin\psi + h_{lnm}^{(t,p,9)}B_x\cos\psi \\ & \left. + h_{lnm}^{(t,p,10)}B_y\sin\psi + h_{lnm}^{(t,p,11)}B_y\cos\psi + h_{lnm}^{(t,p,12)}B_z\sin\psi\right] \end{aligned} \tag{9}$$

Before proceeding further, three important caveats should be highlighted. First, the toroidal/poloidal representation (Equation 2) is divergence-free by construction. While this property is required and thus perfectly appropriate for the magnetic field modeling, in the case of particle flow reconstruction the continuity equation $\partial\rho/\partial t + \nabla\cdot(\rho\mathbf{v}) = 0$ restricts the analysis to only steady-state conditions with $\partial\rho/\partial t = 0$, such that $\nabla\cdot(\rho\mathbf{v}) = \nabla\cdot\mathbf{F} = 0$. Second, as was already realized in the earlier TSE23 and TSEG24 studies, including in the representation Equations 3–9 all terms with every possible combination of the indices n and m is utterly unfeasible because of (a) uneven data distribution in both geometric and parametric space, (b) very high turbulence level in the data, and (b) unreasonably large number of unknown coefficients. All these factors combined would result not only in computationally expensive and unstable inversion algorithms, but also make it hard to distinguish between real features and modeling artifacts. To avoid these complications, we introduce physics-based symmetry conditions, explained in detail below, which greatly simplify the model and effectively eliminate 70%–80% of (virtually redundant) unknown coefficients. Third, in our previously developed magnetic field models TSE23 and TSEG24, the IMF was a principal driving factor, such that the main linear terms in the magnetosheath field expansions were those proportional to IMF B_x, B_y, and B_z. In the present case, the situation is somewhat different: the magnetosheath plasma bulk flow is mainly controlled by the incoming solar wind, always directed along the $X_{\rm GSW}$ axis (by definition oriented antiparallel to the solar wind), while the IMF plays a role of a second-order disturbance factor, modifying the diverging magnetosheath flow lines due to (a) magnetic forces caused by IMF compression/deformation inside the magnetosheath and (b) reconnection phenomena at the boundary.

The difference between the latter two effects entails important implications regarding the model flow symmetry. Namely, when representing the magnetosheath flow deformations due to the IMF compression/tension, the axisymmetric magnetopause can be viewed as an unmagnetized blunt obstacle, such that the flow symmetry properties are entirely dictated by the IMF orientation and have no relation to the magnetospheric magnetic field inside the magnetopause.

Drivers	Coefficients and index limits	F component parities	Parity diagram
F_{sw} $F_{sw}B_x$ $F_{sw}B_y$ $F_{sw}B_z$	$g^{(t)}_{lnm}$ 0; $h^{(t)}_{lnm}$ $2\le n\le N$, $2\le m\le n$ (even m); $g^{(p)}_{lnm}$ $1\le n\le N$, $0\le m\le n$ (even m); $h^{(p)}_{lnm}$ 0	F_x F_y F_z y even odd even z even even odd	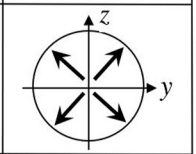
$F_{sw}\cos\psi$ $F_{sw}B_x\sin\psi$ $F_{sw}B_z\cos\psi$	$g^{(t)}_{lnm}$ 0; $h^{(t)}_{lnm}$ $2\le n\le N$, $2\le m\le n$ (even m); $g^{(p)}_{lnm}$ $1\le n\le N$, $0\le m\le n$ (even m); $h^{(p)}_{lnm}$ 0	F_x F_y F_z y even odd even z even even odd	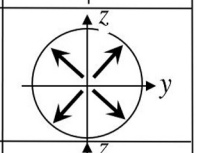
$F_{sw}B_y\cos\psi$	$g^{(t)}_{lnm}$ $1\le n\le N$, $0\le m\le n$ (even m); $h^{(t)}_{lnm}$ 0; $g^{(p)}_{lnm}$ 0; $h^{(p)}_{lnm}$ $2\le n\le N$, $2\le m\le n$ (even m)	F_x F_y F_z y odd even odd z odd odd even	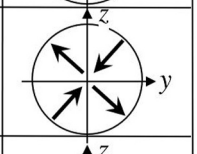
$F_{sw}\sin\psi$ $F_{sw}B_xB_z$ $F_{sw}B_x\cos\psi$ $F_{sw}B_z\sin\psi$	$g^{(t)}_{lnm}$ 0; $h^{(t)}_{lnm}$ $1\le n\le N$, $1\le m\le n$ (odd m); $g^{(p)}_{lnm}$ $1\le n\le N$, $1\le m\le n$ (odd m); $h^{(p)}_{lnm}$ 0	F_x F_y F_z y even odd even z odd odd even	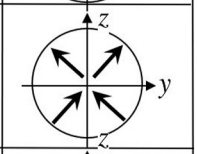
$F_{sw}B_xB_y$ $F_{sw}B_y\sin\psi$	$g^{(t)}_{lnm}$ $1\le n\le N$, $1\le m\le n$ (odd m); $h^{(t)}_{lnm}$ 0; $g^{(p)}_{lnm}$ 0; $h^{(p)}_{lnm}$ $1\le n\le N$, $1\le m\le n$ (odd m)	F_x F_y F_z y odd even odd z even even odd	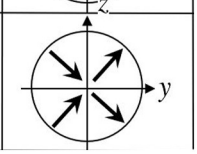

Figure 2. Explaining the hierarchy of model expansion terms, their index limits, and the flux component parities, graphically illustrated in the diagrams on the right. In the left column, interplanetary drivers unrelated/related to the reconnection are shown in black/red fonts, respectively.

By contrast, the reconnection effects depend on the mutual orientation of IMF and the underlying magnetospheric field, which makes it necessary to include in the expansions Equations 8–9 terms controlled by the geodipole tilt angle ψ. The above considerations are summarized in Figure 2 in the form of a table on the left and parity diagrams in the rightmost column. The driving terms in the left column fall into two groups: (a) Those unrelated to the reconnection (shown by black font), and (b) reconnection-related terms that depend both on IMF components and on the geodipole tilt angle ψ (shown in red).

The first row corresponds to four groups of terms, including the solar wind particle flux F_{sw} and its products with three IMF components. All these terms are unrelated to reconnection and represent a radially diverging antisunward flow, symmetric with respect to both equatorial and noon meridian planes, as illustrated in the last column diagrams. The coefficients $g^{(t)}_{lnm}$ and $h^{(p)}_{lnm}$ are entirely omitted from this group (marked by zeros), because the corresponding terms do not satisfy the required symmetry conditions and, hence, only even m values are allowed. Under each of the four coefficients the starting/ending values of n and permitted m index parities are shown, such that redundant zero terms be excluded from the expansions.

The next row includes an IMF-independent term $F_{sw}\cos\psi$, whose role is to take into account tilt-related changes of the magnetopause shape, mirror-symmetric about the equatorial plane. Two other terms, $F_{sw}B_x\sin\psi$ and $F_{sw}B_z\cos\psi$ are responsible for the reconnection effects and, hence, include sines and cosines of the tilt angle ψ. The reconnection-associated flow geometries and parities for each term can be qualitatively understood by overlaying each of three IMF components onto subsolar magnetospheric field lines of a perpendicular ($\psi = 0$) or parallel ($\psi = 90°$) dipole field, shielded within an axisymmetric magnetopause. For example, in the case of a purely azimuthal IMF B_y and perpendicular dipole (3rd row in Figure 2), the term $F_{sw}B_y\cos\psi$ represents the outward transport of reconnected magnetic flux tubes with frozen-in plasma in the northern-dawn and southern-dusk sectors (2nd/4th quadrants, resp.), accompanied with an oppositely directed transport in the northern-dusk and southern-dawn sectors (1st/3rd quadrants). This is exactly the convection type, responsible for the asymmetric magnetic flux loading in the tail lobes, which results in the nightside plasma sheet twisting under the

Table 1
Magnetosheath/Magnetosphere Data Set: Contributing Missions, GSW Latitude/LONGITUDE Range, Numbers of Records, Timespans

Mission	Lat min (degs)	Lat max (degs)	Lon min (degs)	Lon max (degs)	Number of Records	Begin date (year/doy)	End date (year/doy)
Cluster 1	−89.0	73.3	−117.1	115.9	70,762	2001/033	2004/170
Cluster 3	−88.7	68.5	−121.0	119.4	70,076	2001/035	2009/129
Cluster 4	−83.8	73.0	−125.8	132.4	568,856	2001/033	2022/171
Themis A	−31.0	32.1	−105.6	100.5	160,015	2008/149	2024/144
Themis B	−32.6	24.7	−115.5	114.1	3,951	2008/097	2009/358
Themis C	−24.7	19.4	−110.6	117.0	18,525	2007/139	2010/009
Themis D	−27.3	27.9	−101.9	97.0	132,373	2007/161	2024/144
Themis E	−27.2	29.0	−100.1	93.8	71,312	2007/161	2024/114
MMS–1	−51.8	34.1	−122.4	126.4	266,249	2015/245	2024/142
				Total:	1,362,119		

influence of IMF B_y (Cowley, 1981; Owen et al., 1995; Russell, 1972; Sibeck et al., 1985; Tsyganenko, 1990; Tsyganenko et al., 1998).

The 4th and 5th rows include both reconnection-related and unrelated drivers that affect the flow components in the north-south and dawn-dusk directions. The term $F_{sw} \sin\psi$ is the tilt-antisymmetric counterpart of the IMF-independent term in the second row; the terms containing the cross products B_xB_y and B_xB_z induce, respectively, dawn-dusk and north-south asymmetries in the IMF draping at cone angles intermediate between those for strictly parallel and perpendicular IMF orientations. In particular, the dawn-dusk asymmetries associated with B_xB_y correspond to the common Parker and ortho-spiral IMF structures; that kind of asymmetry was addressed in many simulations and data-based studies (e.g., Samsonov, 2006; Walsh et al. (2012) and refs. therein). In the present modeling experiment, we assumed $L = 2$ and $N = 8$ as the upper summation limits in (Equation 7). Given all the symmetry/parity limitations listed in Figure 2, this resulted in a total of 1632 unknown coefficients to be derived from the data.

Next, note that the flow vector expansions Equations 3–9 are quantified by the external input not only via the parameters F_{sw}, IMF B_x, B_y, B_z, and ψ, listed in the first column of the table in Figure 2, but also by the magnetopause subsolar standoff distance R_S and the flaring parameter α, entering in the coordinate δ in (Equation 1). These two parameters were assumed as functions of the solar wind ram pressure P_d and IMF B_z, determined for each data record using a previously developed model approximation (TSEG24, Equation 3):

$$R_S = R_{S_0}\left[(P_d/2)^{\varepsilon} + \gamma(B_z/10)\right], \qquad \alpha = \alpha_0 + \Delta\alpha \exp(-B_z 10), \tag{10}$$

Calculation of the parameter values entering in (Equation 10) was made in TSEG24 using (a) the 2D magnetosphere-magnetosheath data selection diagrams (similar to those in Figures 4–7 in the next section below) and (b) a "dynamical weighting" of data, performed at every step of the nonlinear fitting of the magnetic field model. In the present study, we use the following specific values obtained in TSEG24 for the training data set: $R_{S_0} = 11.1\,R_E$, $\varepsilon = 0.16$, $\gamma = -0.08$, $\alpha_0 = 0.49$, and $\Delta\alpha_0 = 0.22$ (TSEG24, Table 2). For all the remaining details of the procedure, the reader is referred to the above cited open-access publication.

3. Data

The 1-min plasma and magnetic field data used in this study are mostly the same as those used in TSE23 and TSEG24, but with two differences. First, a portion of the most recently published data for the period 2022–2024 has been appended to the previously used data set (2001–2022). Specifically, for Themis A, D, and E probes, the newly added data cover the interval from 11/01/2022 to 05/22/2024; for MMS-1: from 10/20/2022 to 05/21/2024; for Cluster 4: from 01/01/2022 to 09/30/2022 (a more detailed summary of the data used to create the model is also given in Table 1 below). Second, since the Geotail CPI solar wind

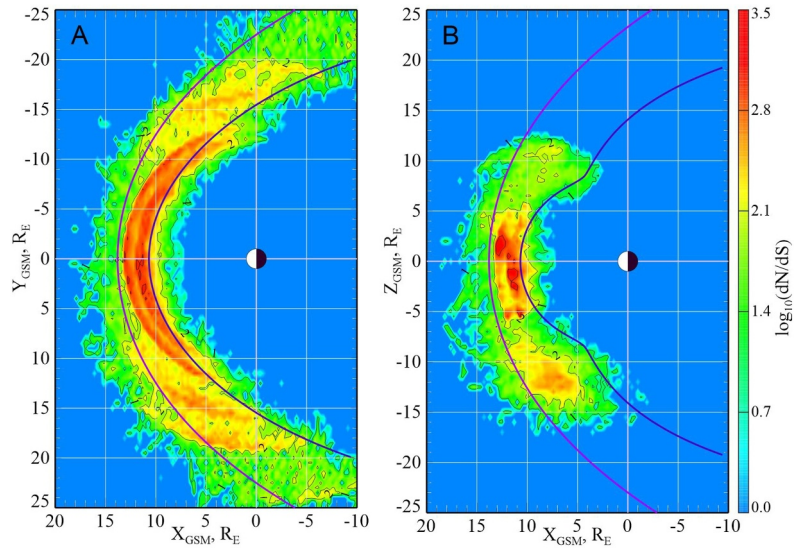

Figure 3. Equatorial (a) and meridional (b) diagrams of the data coverage of the modeling region. The one-minute data points are selected from 30°-wide spherical sectors centered on $Y_{GSM} = 0$ and $Z_{GSM} = 0$ planes, respectively, rotated into the center planes, and binned into $dS = 0.5 \times 0.5\,R_E$ squares. The color coding quantifies the coverage density by the logarithm of the point numbers dN in each bin. Nominal magnetopause and bow shock sections are shown with dark blue and purple contours, respectively.

plasma analyzer (unlike its magnetometer) did not fully operate in the magnetosheath, its data were completely excluded from the present study.

The spatial coverage of the employed data base is illustrated in Figure 3 in the form of equatorial (panel A) and meridional (panel B) diagrams of data density distributions. Since the nightside magnetosheath plasma and magnetic field become increasingly turbulent at larger distances from the subsolar area, the data tailward limit was restricted by $X_{GSM} \geq -10\,R_E$. The data in each diagram were selected from spherical sectors with angular

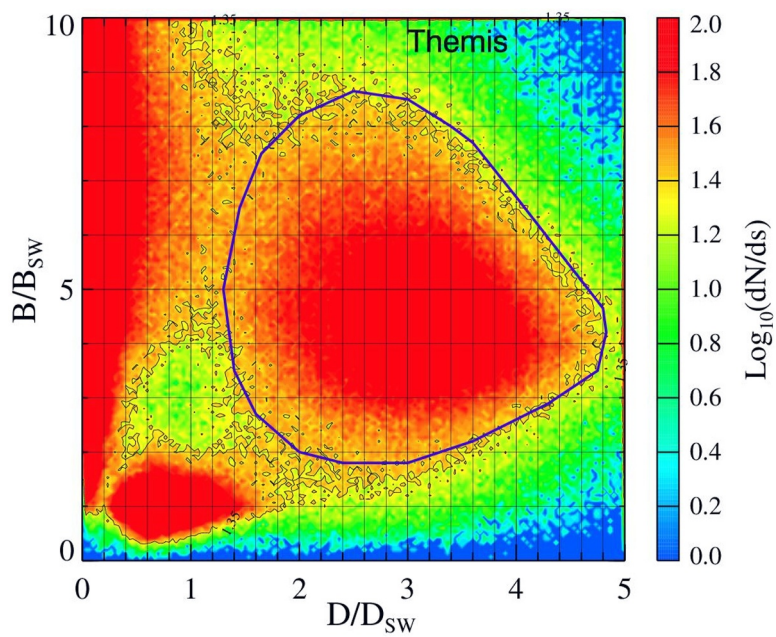

Figure 4. The D/D_{sw} versus B/B_{sw} diagram, illustrating Themis A, B, C, D, E magnetosheath data selection, based on Jelinek et al. (2012) method. Heavy closed line encircles the area associated with the magnetosheath region.

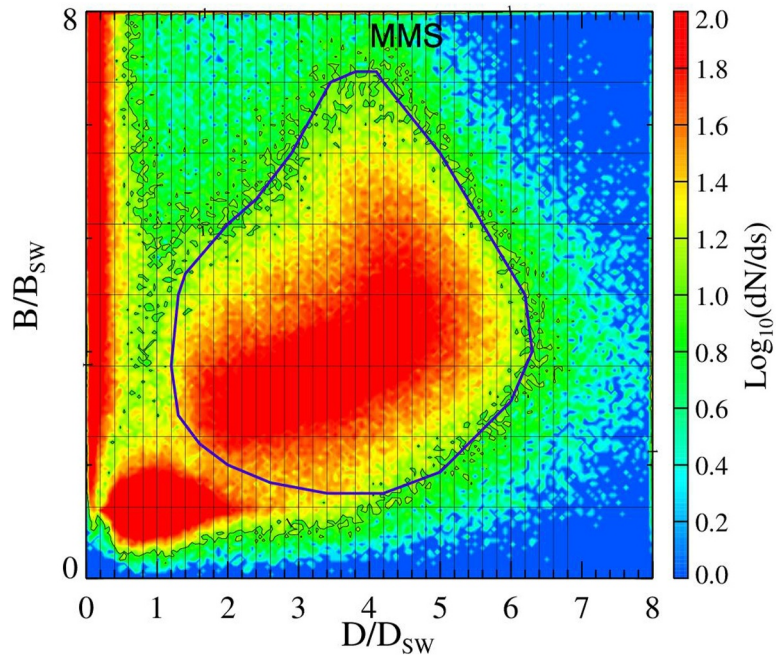

Figure 5. Same as in Figure 4, but for MMS-1 data.

halfwidth 15°, centered at $Z_{GSM} = 0$ (panel A) and $Y_{GSM} = 0$ (panel B) planes, respectively. Each data point was rotated into the corresponding center plane and binned there into a set of $dS = 0.5 \times 0.5\ R_E$ squares.

The data density distributions were quantified by $d = \log_{10}(dN/dS)$ of the numbers dN of data points that fell into each bin, presented in the plot in the form of color-coded maps (to avoid singularities in no-data areas, empty bins with $dN = 0$ were assigned with $d = 0$). Comparison of the panels shows a strong difference between the low- and high-latitude coverage. The near-equatorial data (panel A) fill the entire space between the nominal

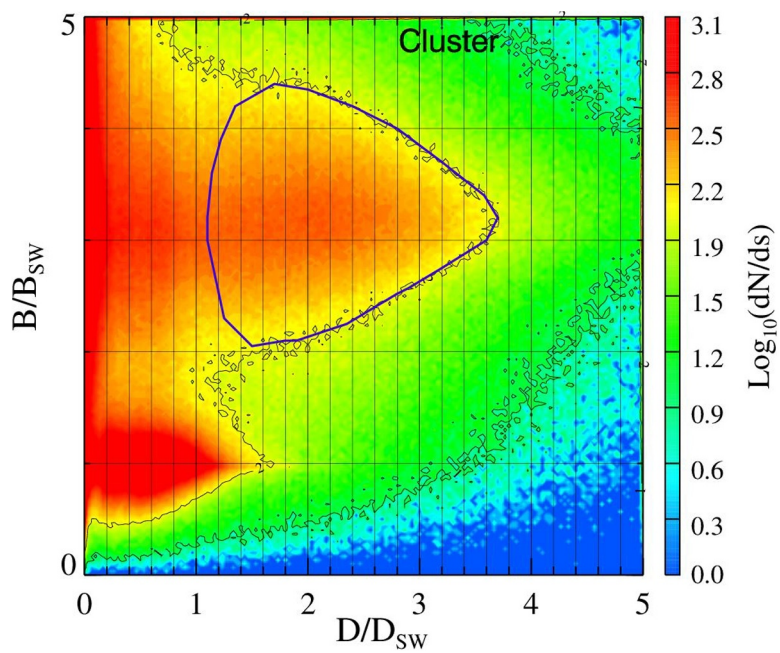

Figure 6. Same as in Figures 4 and 5, but for Cluster 1, 3, and 4 data. Note the lack of a distinct gap between the magnetosheath and magnetosphere areas, clearly visible in the previous plots for Themis and MMS data.

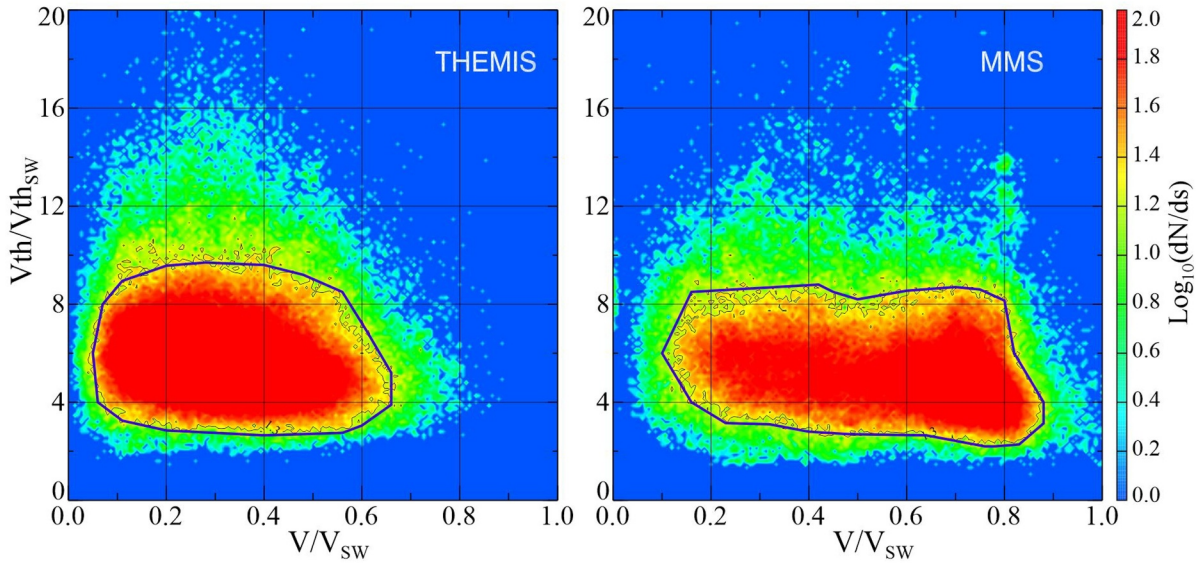

Figure 7. Vth/Vth_{sw} versus V_b/V_{sw} diagrams for Themis (left) and MMS (right). As in the previous figures, the solid closed lines encircle the area associated with the magnetosheath.

magnetopause and bow shock, calculated using Lin et al. (2010) and Lu et al. (2019) models (shown by blue and purple lines in both panels). The largest data density in the red crescent-shaped area on the dayside is mostly due to the contribution from Themis A, D, and E probes with apogees between 11 and 13 R_E. By contrast, the data around the meridional plane (panel B) almost entirely concentrate on the dayside. The northern hemispace data do not extend above latitudes 60–63°; in the southern sector, the latitude range is larger and reaches the terminator plane, due to the highly inclined Cluster orbit. However, even there the coverage is far from uniform and gets progressively scarcer at latitudes higher than ∼− 66°. As discussed below, the lack of high-latitude data substantially limits the latitudinal range of the modeling.

As in our two previous studies, the newly updated data pool was first subject to a rough selection, based on average magnetopause and bow shock models, respectively compressed and expanded by a factor 1.4. At the second stage, a two-step filtering procedure was applied, using a modification of the diagram method by Jelinek et al. (2012). Specifically, at the first step the data points were plotted as a 2D diagram of the proton densities D and magnetic field magnitudes B, normalized by concurrent values D_{SW} and B_{SW} in the incoming solar wind. Three densely grouped areas of enhanced data point concentration can be immediately identified, corresponding to the magnetosphere (low D, high B), solar wind (low D, low B), and the magnetosheath (high D, intermediate B). The magnetosheath data subset was created by encircling its area on the diagram with a polygon and applying a winding selection algorithm. Although the procedure has already been described in TSE23 and TSEG24, we briefly reproduce its results here, in view of the recent data update and in order to keep the paper more or less self-contained.

Figures 4–6 illustrate the D –B selection of Themis, MMS, and Cluster data. The assigned shapes and sizes of the selection polygons are inevitably somewhat subjective, especially in the case of Cluster (Figure 6), whose orbits spent relatively much time in the outer polar cusps where plasma and field properties are rather similar to those in the magnetosheath. For that reason, there is no distinct clearance nor isthmus between the magnetosheath and magnetosphere data of Cluster, such that the dividing line in Figure 6 was drawn based on purely visual criteria.

At the next step, another round of filtering was applied to the data selected at the first step by means of the above D/D_{sw} versus B/B_{sw} diagrams. In this case, a similar diagram method was used, but with the normalized proton bulk speed V_b/V_{sw} and thermal speed Vth/Vth_{sw} as the selection parameters. This kind of filtering was applied to only Themis and MMS data, because of the already mentioned ambiguity in distinguishing cusp and magnetosheath data in Cluster's observations. Figure 7 shows the corresponding Vth/Vth_{sw} versus V_b/V_{sw} diagrams for Themis (left) and MMS (right) data. In this selection step, the filtering contour was drawn in order to leave out the

data with $Vth/Vth_{sw} \geq 9-10$, most likely associated with the outermost magnetosphere or low-latitude magnetopause with proton energies by two orders of magnitude larger than in the solar wind.

Again, this interpretation and the contour placement may appear subjective; however, in any case a possible loss of some portion of the magnetosheath data is insignificant (around 10%) and, based on the size of final data subsets (on the order of half million records), is unlikely to result in an overfitted model.

Table 1 provides principal information of the final data set, generated as a result of the two-step selection/refinement procedure. Its format is similar to that of Table 1 in TSE23, but the numbers are different due to the added most recent data, the double filtering, and the absence of Geotail data. About half of the total 1,362,119 records are contributed by three Cluster probes (709,694 records).

Following the approach of our two previous studies, the entire data set was again split into training (T) and validation (V) subsets, in which all consecutive data were alternately separated by contiguous 10-day intervals, thus ensuring their independence. The respective sizes of thus generated T and V subsets were found nearly equal: 685,260 and 676,859 one-minute records. Finally, before calculating the model parameters, the data in both subsets underwent the last round of filtering: namely, in order to avoid abnormal interplanetary conditions and extreme magnetospheric states, all data records with principal solar wind parameters outside their 5%–95% percentiles were excluded. More specifically, the IMF components were limited to $|B_x| \leq 5.5$, $|B_y| \leq 6.0$, and $|B_z| \leq 5.0$ nT, the solar wind proton density, bulk speed, and ram pressure were restricted to $2 \leq N_p \leq 15$ cm^{-3}, $300 \leq V_{sw} \leq 600$km/s, $0.5 \leq P_{dyn} \leq 4.5$nPa, and Alfvénic and magnetosonic Mach numbers were limited to $4.5 \leq MA \leq 19.0$ and $3.8 \leq Ms \leq 7.5$, respectively. Also, all vector quantities were transformed from the standard GSM into GSW (magnetospheric solar-wind) coordinates, with X-axis directed antiparallel to the currently observed solar wind flow. Due to all the restrictions, the final size of the T and V subsets for the model fitting further decreased to 417,404 and 417,329 one-minute records, respectively.

4. Results

The above described plasma flow model with 1632 free coefficients was fitted to the data using a standard SVD algorithm with the tolerance parameter equal to $5{\cdot}10^{-6}$ (the inverse condition number, i.e., the ratio of the smallest to the largest singular value, see Press et al., 1992, Ch.2.6). As usual, we define the fitting target function as the residual r.m.s. deviation of the model flow from the observed one: $Q = \left\{\langle(\mathbf{F}_{\rm mod} - \mathbf{F}_{\rm obs})^2\rangle\right\}^{1/2}$, such that the measure of the fitting quality is the ratio $Q/\mathcal{F}$ where $\mathcal{F} = \left\{\langle\mathbf{F}^2_{\rm obs}\rangle\right\}^{1/2}$ is the observed r.m.s. Flow magnitude over the modeling data subset. For the T and V subsets, the obtained $Q/\mathcal{F}$ values were found, in percent, equal to 39.2% and 42.3%, respectively. These values are notably better (lower) than those obtained in the magnetosheath magnetic field modeling in TSE23 and TSEG24 (around 50%–60%), which is what one could expect, given the more orderly and smooth patterns of the plasma bulk flow, in comparison with more turbulent and strongly IMF-dependent magnetic fields in the same region.

Before going to the model flow patterns, we present in Figure 8 the scatter diagrams between the observed and modeled flow components F_x, F_y, and F_z, illustrating the fitting quality.

The flow values are in units 10^8 cm^{-2} s^{-1} (for reference, equivalent to a flow with particle density of 2.0 cm^{-3} and speed of 500 km/s) and the top/bottom rows correspond, respectively, to the training (T) and validation (V) subsets. For the T subset, the regression slopes S and Pearson correlations R for all three flow components are remarkably high, in the range $S = 0.98$–1.00 and $R = 0.82$–0.91. As expected, almost all data points in the F_x diagrams (left panel) concentrate in the 3rd quadrant, indicating the overwhelming dominance of antisunward bulk flows in the magnetosheath (a small group of data points in the 4th quadrant with $F_x > 0$ may belong to sunward foreshock flows). Because of the lowest variation range and the highest scatter about the regression line, that component has the smallest correlation between the model and data ($R = 0.824$). The center panel for the dawn-dusk flow F_y demonstrates the best performance of the model for that component, with $R = 0.905$. This is what one should naturally expect, based on much wider coverage of the near-equatorial region (panel A in Figure 3) in comparison with the relatively narrow meridional data distribution (panel B, the same Figure). The correlation value for the north-south component F_z (right panel) is intermediate ($R = 0.836$) between those for F_x and F_y, but the highest slope ($S = 0.998$). Note the significantly larger size of the data cloud in the 3rd quadrant,

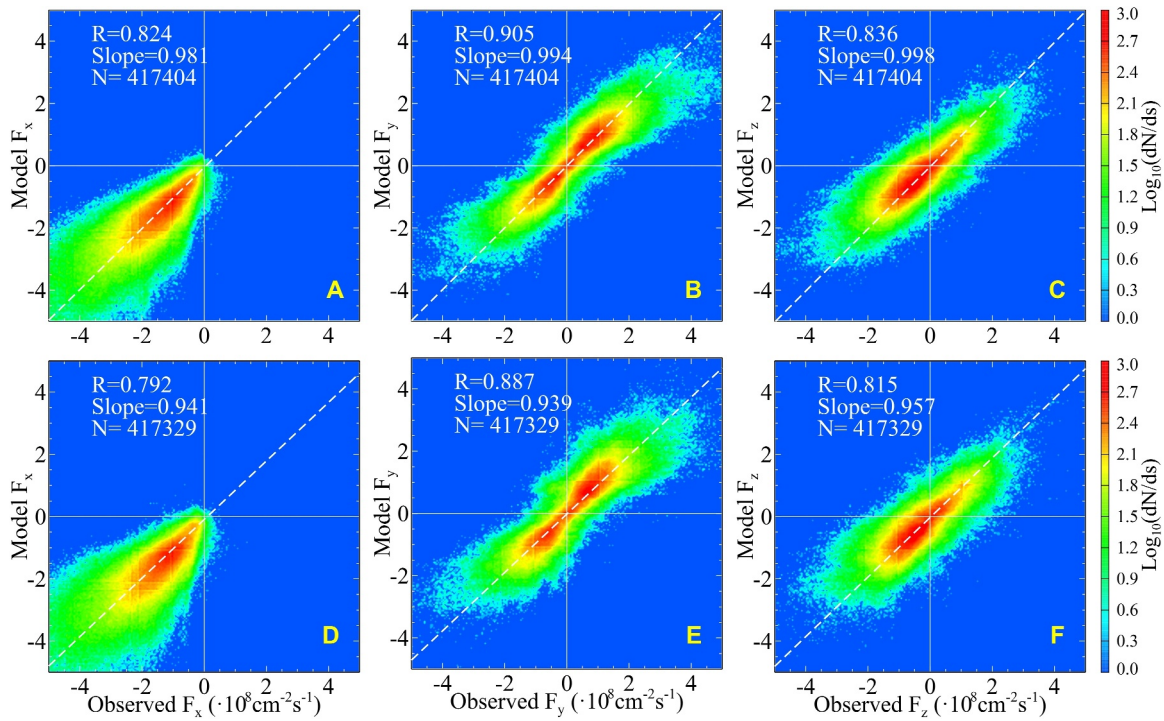

Figure 8. Scatter plots of model against observed flow components. Top and bottom rows correspond to the training and validation subsets. Letters A/D, B/E, and C/F correspond to F_x, F_y, and F_z flow components, respectively.

reflecting a strong north-south asymmetry of Cluster's orbital coverage, whose apogees lie far southward from the equatorial plane (panel B in Figure 3).

As shown in the bottom row of Figure 8, the slopes and correlation values for the validation set are somewhat lower than those for the training subset, as it normally should be. The difference, however, is not large, which indicates that the degree of the model's complexity is not far from the optimum (see Gershenfeld, 2003, Ch.12.4), such that the assumed summation limits $L = 2$, $N = 8$ in Equations 3 and 7 do not result in a tangible over- or underfitting.

Figure 9 shows two diagrams of the plasma flow around the magnetosphere in the equatorial plane, derived from the model using nominal solar wind conditions ($V = 400$ km/s, $N_p = 5\,\mathrm{cm}^{-3}$, $F_{\mathrm{sw}} = 2 \cdot 10^8\ \mathrm{cm}^{-2}\ \mathrm{s}^{-1}$), untilted geodipole ($\Psi = 0$), and purely transverse IMF with $B_x = B_y = 0$. Panels A and B correspond, respectively, to purely northward ($B_z = +5$ and southward $(B_z = -5)$ IMF orientations. The magnetopause (blue contour) in this and following plots corresponds to the model surface $\delta = 0$ given by Equation 1 with R_S and α from Equation 10, and the bow shock trace (purple) is based on the empirical model by Lu et al. (2019). Note here that our magnetosheath flow model, by construction, has no sharp boundaries and both contours are given only for the reader's orientation.

In both diagrams, one can see a stagnation of the plasma flow in the subsolar area, changing into a gradual increase away from the Sun-Earth line, especially visible on approaching the terminator and further tailward. The subsolar stagnation is clearly more pronounced in the diagram B for the southward IMF, where, according to Equation 10, the magnetopause is shifted earthward by $\sim 0.9\,R_E$ from $R_S = 11.6\,R_E$ to $10.7\,R_E$. In that case, the flow stagnation area expands sideways, such that the pre-noon and post-noon flow acceleration regions shift to the terminator plane. Note also that the flow vectors in both diagrams are not strictly tangential to the model magnetopause, but have a tangible inward normal component. Although that can be partially ascribed to the inevitable data scatter and model imperfections, note that the plasma 'penetration' is clearly stronger in the case of southward IMF, which may well be an effect of the classical Dungey-type reconnection at the magnetopause. However, given all the weaknesses of the method, the conjecture cannot be uniquely and unambiguously confirmed in the framework of the data-constrained modeling.

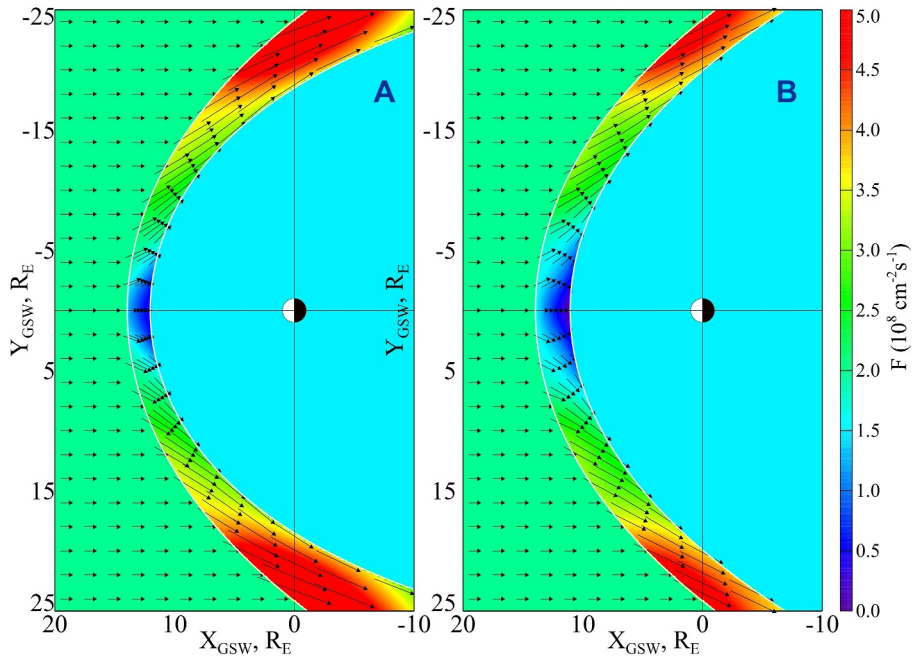

Figure 9. Equatorial diagrams of the plasma flow around the magnetosphere for purely transverse interplanetary magnetic field (IMF) orientation with $B_x = B_y = 0$. Panels A and B correspond to northward ($B_z = +5$nT) and southward ($B_z = -5$nT) IMF. The solar wind and magnetosheath flows are displayed with arrows and the color coding is in units 10^8 cm^{-2} s^{-1}.

Figure 10 shows in a similar format the plasma flow distribution in the noon meridional plane. Unlike in the previous Figure 9, the plots are limited to only the dayside, due to virtually no high-latitude data at the nightside and, hence, invalid model results in that region. Also, because of lower meridional values, the maximum of the flow color scale is reduced here from $5 \cdot 10^8$ to $3 \cdot 10^8$ cm^{-2} s^{-1}. To give the reader at least a rough idea of the

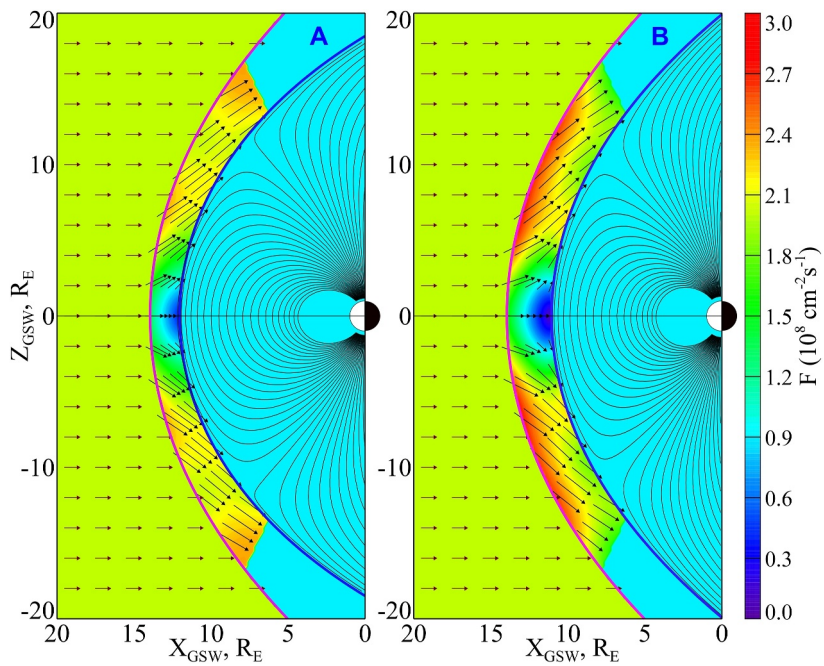

Figure 10. Plasma flows in the meridional plane. Panels A and B correspond to interplanetary magnetic field $B_z = +5$ and $B_z = -5$, respectively.

dayside cusp positions, a set of TA15 quiet-time field lines (Tsyganenko & Andreeva, 2015) was overlaid onto each plot (in view of a different magnetopause shape used in that model, a non-uniform separate re-scaling was applied along X and Z axes, to better fit the lines into the Shue-type boundary). In addition, the color coding and flow arrows are limited to the latitude interval within ±68°, covered with data (see panel B in Figure 3). Since the data density rapidly drops to zero beyond that interval, the model destablilizes at higher latitudes and produces unphysical sunward flows; these artifacts are not shown and the no-data areas are filled with the same uniform color as inside the magnetopause. As in the equatorial diagrams in Figure 9, one again sees a stagnation region at low latitudes, more distinct and spatially extended in the case of negative IMF B_z. Also, the flow acceleration toward the cusps is significantly stronger in the latter case, which may be attributed to the formation of northward and southward plasma streams away from the equatorial plane, associated with reconnection at the magnetopause.

To further illustrate the IMF effects upon the flow geometry, the next Figure 11 shows distributions of the plasma flow in the vicinity of the model magnetopause for nominal solar wind conditions with $F_{sw} = 2 \cdot 10^8$ cm^{-2} s^{-1}, perpendicular orientation of the IMF with $B_\perp = 5$nT, $B_x = 0$ (i.e., cone angle $\theta = 90°$), and three clock angles: $\phi = 0°$ (A), 90° (B), and 180° (C). The initial idea behind creating those diagrams was to try to find signatures of the magnetic field influence on the plasma flow near the magnetopause, which is believed to critically depend on the mutual orientation of IMF in the incident solar wind and the terrestrial field inside the boundary (Erkaev et al., 1998, 2006; Phan et al., 1994; Pudovkin et al., 2001; Pudovkin & Semenov, 1985; Siscoe et al., 2002; Wang et al., 2004).

For all three clock angles in Figure 11, one sees a significant deceleration of the flow in the subsolar area, with F below $\lesssim 10^8$ cm^{-2} s^{-1}, that is, less than half of that in the solar wind ($F_{sw} = 2 \cdot 10^8$ cm^{-2} s^{-1}). The most interesting feature (persistent from one numerical experiment to another) is the spatial evolution of the flow retardation area. More specifically, in the case of a purely northward IMF (top diagram A), the flow isointensity contours are slightly elongated in the dawn-dusk direction (i.e., normal to both IMF and underlying magnetospheric field). In the middle diagram B, corresponding to the purely dawn-dusk IMF, the stagnation area is more elongated and somewhat inclined to the Z axis. Finally, as the IMF becomes purely southward (panel C), the flow retardation area further expands along Y axis, but contracts in Z direction, and thus develops into a highly stretched stagnation region, manifesting the formation of a transverse stagnation line, usually associated with the interplanetary magnetic flux injection rate and the cross-polar potential drop (e.g., Siscoe et al., 2002).

The above described effects agree well with a traditional view of the global magnetospheric convection, dating back to the Dungey's seminal concept. Based on this paradigm, northward IMF conditions lead to the magnetic flux pile-up in front of the dayside magnetopause and, due to the dusk-dawn electric field, increase the transparency of the boundary for the incoming plasma flow. By contrast, southward IMF launches reconnection in the subsolar region and intensifies large-scale tangential flows at the subsolar magnetopause. At the same time, the dawn-dusk electric field associated with the merging initiates sunward plasma flows from inside the magnetosphere, directed against the incoming flow. This results in a weaker plasma transport across the magnetopause, manifested as the wide dark area in the bottom panel C of Figure 11.

5. Discussion: Dipole Tilt Effects

From a theoretical viewpoint, the seasonal/diurnal variations of the geodipole orientation should affect the magnetosheath flows in two ways. First, the magnetopause shape, especially around the outer cusps, is dipole tilt-dependent (e.g., Boardsen et al., 2000; Lin et al., 2010) and, hence, must result in modifications of the flow in a purely hydrodynamic sense. Second, and more important, the dipole tilt changes the magnetic field configuration just inside the dayside magnetopause and, together with the IMF draping, defines the distribution of field merging areas on the magnetopause (e.g., Fuselier et al., 2024), thereby affecting the global flow geometry.

In view of these considerations, it is of interest to visualize the dipole tilt effects as inferred from the present modeling. Figure 12 shows two meridional sections of the magnetosheath flow, similar to those in Figure 10, but for the maximum dipole tilt $\psi = 30°$. The left and right plots correspond to opposite orientations of IMF: $B_z = +5$nT (A) and $B_z = -5$nT (B). As in Figure 10, due to the lack of high-latitude magnetosheath data, both plots are limited to the same GSW latitude range between $\sim -70°$ and $\sim +60°$. In both cases, the patterns are strongly asymmetric about equator and reveal interesting and significant changes from the corresponding untilted distributions shown in Figure 10. First, the flow magnitudes are generally larger in the case of southward IMF.

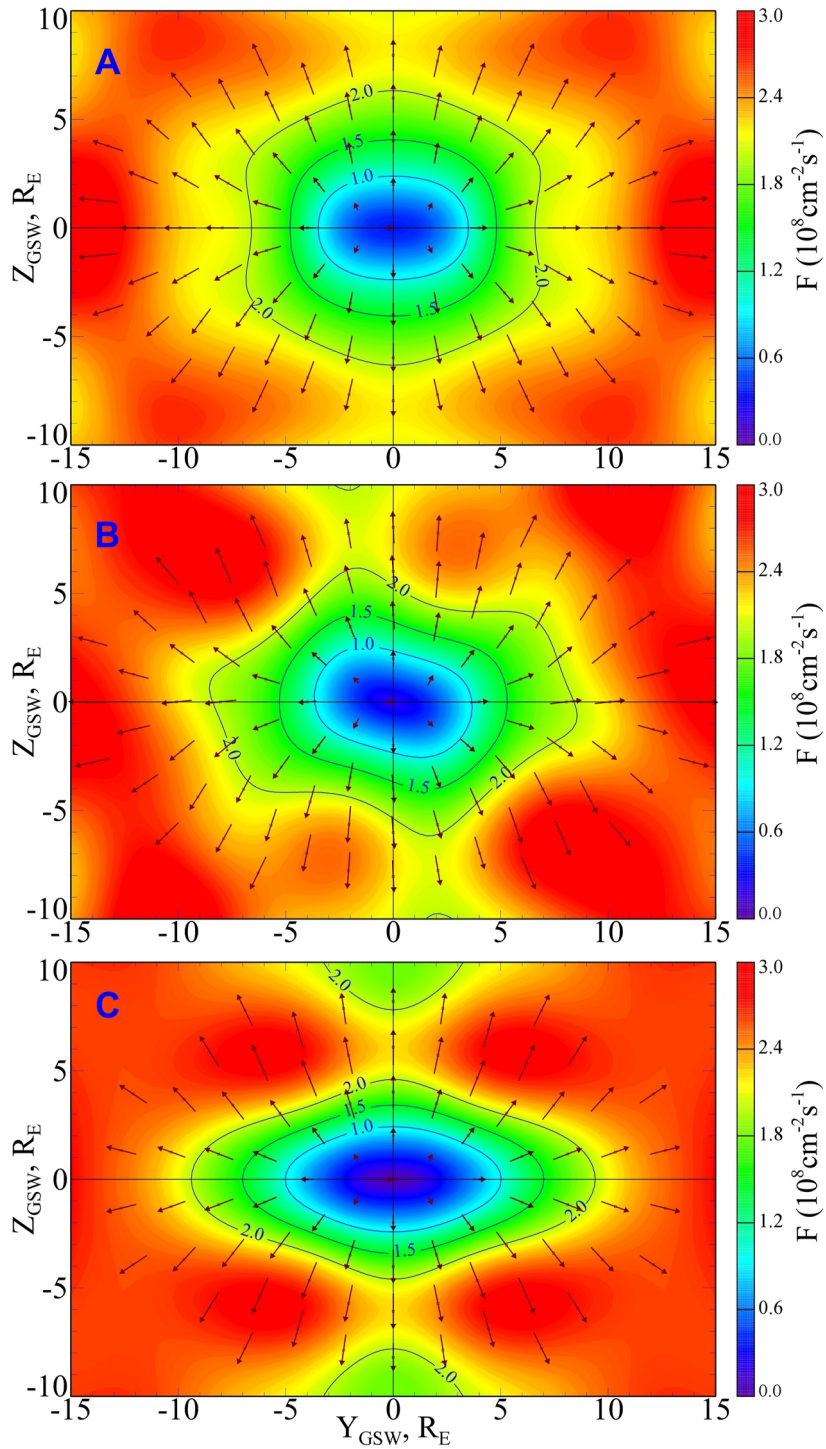

Figure 11. Diagrams of the plasma flow around the dayside magnetopause in $Y - Z$ projection (i.e., as viewed from Sun). Panels A, B, and C correspond to interplanetary magnetic field $B = 5$nT, cone angle 90°, and three clock angles equal to 0, 90, and 180°, respectively.

Second, in both panels the subsolar flow stagnation areas are shifted southward from the equatorial plane, in agreement with a similar tilt-related shift of the reconnection site in an MHD simulation by Eggington et al. (2020). Third, in the case of negative IMF B_z (right panel B) an even deeper stagnation area develops poleward of the northern cusp throat. This can be interpreted as a result of the flow braking against the local

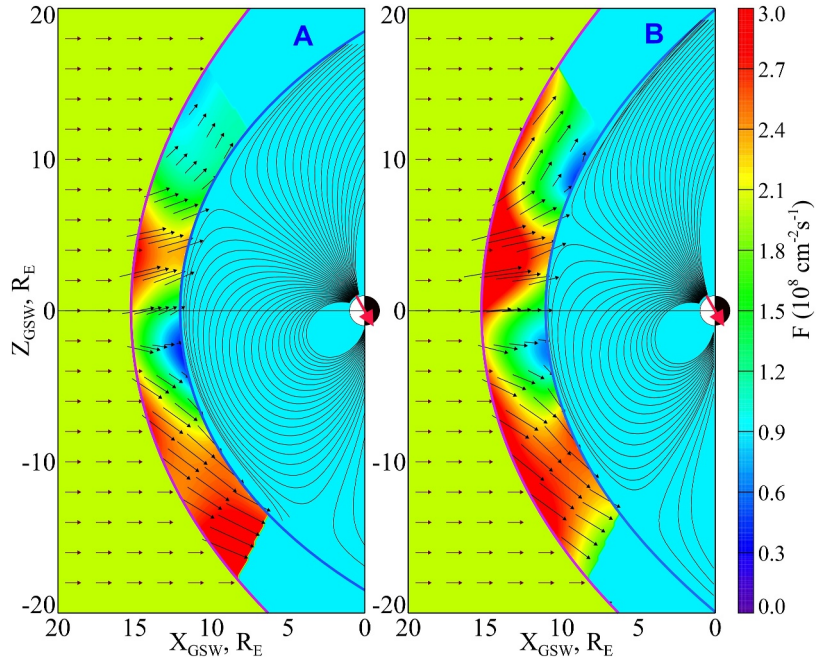

Figure 12. Flow diagrams for purely northward (a) and southward (b) interplanetary magnetic field, corresponding to the tilted geodipole (red arrows) with $\psi = 30°$.

magnetic "wall" at the indented magnetopause (Sotirelis & Meng, 1999; Tsyganenko & Russell, 1999), that forms at the poleward boundary of the outer cusp (not present in the axisymmetric Shue-type model surface used in this study). A similar effect may be present in the southern hemispace; however, its detection is hardly possible because, due to the positive dipole tilt angle, the cusp throat is shifted there to much higher latitudes and larger distances, far beyond the region of the data coverage and, hence, of the model validity.

The above discussed tilt effects are more clearly visible in the diagrams of the plasma flow configuration in a close vicinity of the magnetopause (at $\delta = 0$), shown in the next Figure 13 in the same format as in Figure 11. For the purely northward IMF (panel A), the flow pattern becomes much wider in longitude than that in the untilted case in Figure 11 and shifts southward by 2–3 R_E. In the case of purely azimuthal IMF with 90° clock angle (panel B), the low-latitude retardation area slightly shrinks in the Z direction, while at the top of the plot one sees the emerging northern cusp-related flow stagnation. Finally, for the purely southward IMF (panel C) the low-latitude depression further shrinks in Z, while the northern cusp stagnation deepens and becomes even more pronounced than in the subsolar area.

We note here in passing that, by the model's construction (see Figure 2 and Equations 8 and 9), the tilt effects are mirror-symmetric with respect to the polarity of the tilt angle ψ.

The exact nature of the tilt- and IMF B_z-related relocation of the stagnation areas still remains a subject of discussion. In the case of northward IMF, the latitudinal shift of the near-equatorial stagnation area can be explained by a relocation in the same direction of the magnetospheric field peak, which increases the plasma pile-up effect and decelerates the flow. In the case of southward IMF, the low-latitude site of the subsolar flow deceleration follows the shift of the field merging site, since this is where the cancellation of antiparallel flows from inside and outside the magnetopause is the most effective, as it is clearly seen in the diverging subsolar flows in panel B of Figure 12. The high-latitude flow depression is most likely due to the already mentioned magnetic "wall," formed at the poleward side of the cusp throat. This wall effect dramatically grows as the IMF turns southward, as a result of the redistribution of the dayside magnetic flux due to its erosion at low latitudes and concurrent accumulation poleward from the cusps. Aside from the real physical factors at play, the effects may be partially due to the simplicity of the reference surface $\delta = 0$, based on the Shue-type model. Being axially symmetric, it does not include the high-latitude indentations associated with polar cusps, whose positions and depths depend on the

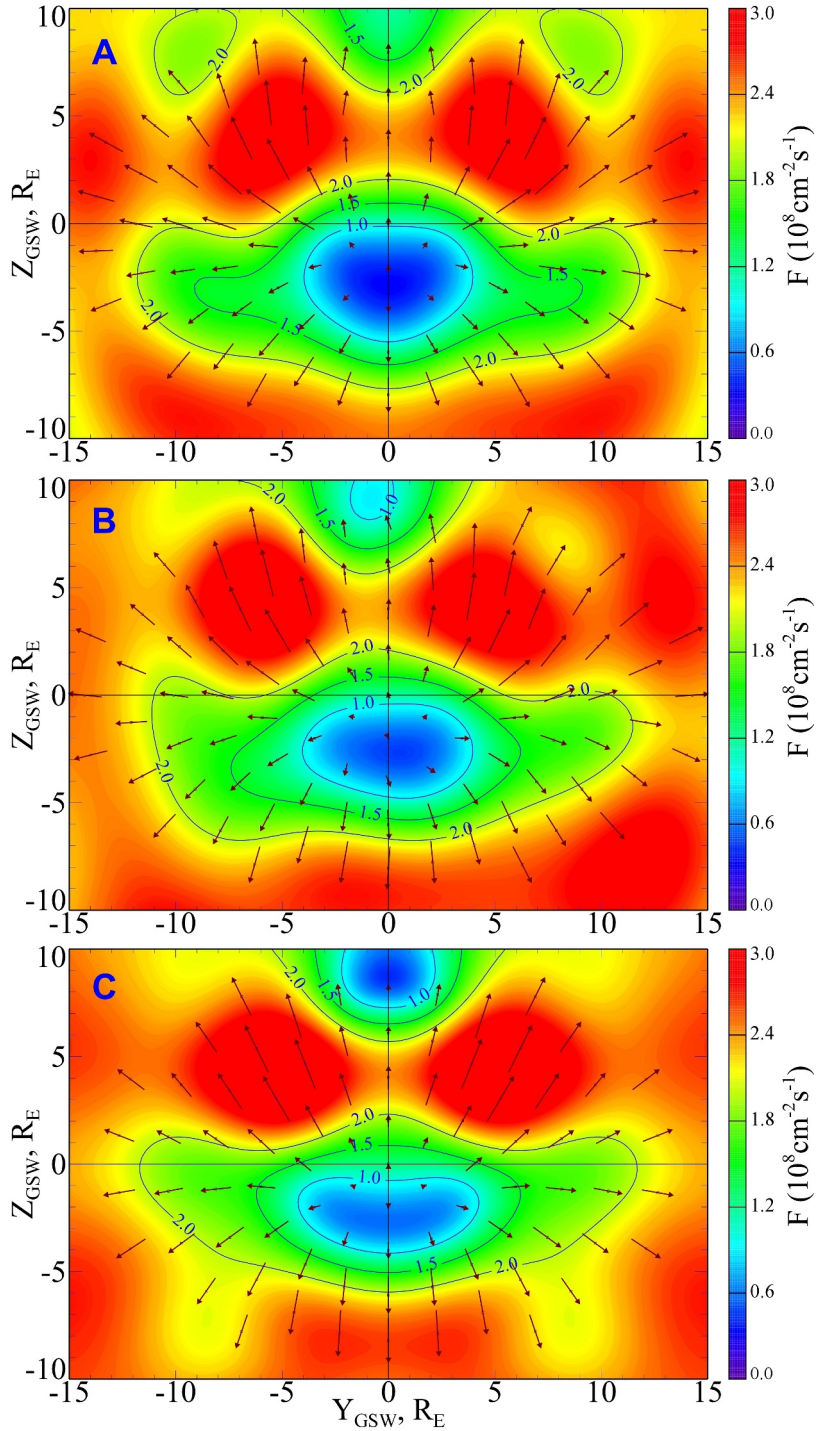

Figure 13. Same as in Figure 11, but for the geodipole tilt $\Psi = 30°$.

dipole tilt (Boardsen et al., 2000; Lin et al., 2010). In the future work, a much more involved study of this issue is planned, based on a more accurate reference boundary.

6. Summary and Outlook

We presented first results of an attempt to quantitatively reconstruct an average large-scale picture of the plasma flow around the magnetosphere, using multi-year sets of in situ spacecraft data combined with concurrent

observations in the interplanetary medium, and an advanced model based on the toroidal/poloidal formalism and steady state assumption. The flow model is driven by the solar wind proton flow, IMF components, and the Earth's dipole tilt angle, in such a way that the IMF parameterization is split into two separate groups with different symmetry and parity properties. The first one is due to the magnetic field compression/tension inside the magnetosheath and, hence, is unrelated to the magnetic field inside the magnetospheric boundary. The second group of IMF effects is associated with the reconnection at the magnetopause and, hence, includes the dipole tilt angle. The modeling demonstrated a satisfactory level of the flow representation in terms of the fitting merit function and model-data scatter plots, confirmed by testing the results obtained for a training subset on an independent validation subset. The modeling revealed regular average patterns of the magnetosheath flow, with the magnitudes of the same order as in the incoming solar wind, but stagnated in the subsolar area and gradually increasing away from the noon sector. The flows are found to be significantly modified by the IMF, reflecting both the magnetic effects due to the presence of the magnetosphere as a hydromagnetic obstacle and those due to the reconnection with the geomagnetic field. Our data-based study confirms quite a substantial impact of the seasonal/diurnal changes of the dipole tilt on the magnetosheath plasma flow geometry. At the same time, it should be realized that the modeling results represent only an average picture, derived from data taken at different times and additionally blurred with inaccuracies in the interplanetary OMNI data due to uncertainties of the propagation time/path from L1 to the Earth's bow shock (e.g., Vokhmyanin et al., 2019). More advanced further studies are definitely needed, including more accurate magnetopause models and more advanced methods of data selection between different geospace domains, using automated AI-based selection algorithms. Also, the diversity of the solar wind types (Borovsky et al., 2019) should be taken into consideration, as well as a delayed/finite-time response of the magnetopause shape and size to changes in the state of interplanetary medium.

Data Availability Statement

Cluster, THEMIS, and MMS magnetometer and plasma instrument data were downloaded from the NSSDC CDAWEB interface at https://cdaweb.gsfc.nasa.gov/cdaweb/index.html. One-minute resolution OMNI data were obtained from SPDF OMNIWEB at https://omniweb.gsfc.nasa.gov. All data sets and software used to obtain the above described results are freely available from the FigShare repository at https://doi.org/10.6084/m9.figshare.27282336.v1.

Acknowledgments
We acknowledge the teams and PIs of all experiments whose data contributed to this study. In particular, Cluster and MMS magnetometer/ephemeris data were obtained from the NSSDC CDAWEB online facility, originally made available by the PIs: A. Balogh and M. Tatrallyay (Cluster data), by J. Burch, C. Russell, and W. Magnus (MMS data). V. Angelopoulos, K.-H. Glassmeier, U. Auster, W. Baumjohann, C. W. Carlson and J. McFadden are acknowledged for the use of THEMIS FGM and ESA data. High-resolution OMNI interplanetary data were obtained from the SPDF OMNIWEB interface (R. McGuire, N. Papitashvili). The authors acknowledge financial support from the Russian Science Foundation Grant 23-47-00084 "Magnetic Reconnection in Space and Laboratory Plasmas: Computer Simulations and Empirical Modeling."

References

Boardsen, S. A., Eastman, T. E., Sotirelis, T., & Green, J. L. (2000). An empirical model of the high-latitude magnetopause. *Journal of Geophysical Research*, *105*(A10), 23–193. https://doi.org/10.1029/1998ja000143

Borovsky, J. E., Denton, M. H., & Smith, C. W. (2019). Some properties of the solar wind turbulence at 1 AU statistically examined in the different types of solar wind plasma. *Journal of Geophysical Research: Space Physics*, *124*(4), 2406–2424. https://doi.org/10.1029/2019JA026580

Cowley, S. W. H. (1981). Magnetospheric asymmetries associated with the y-component of the IMF. *Planetary and Space Science*, *29*(1), 79–96. https://doi.org/10.1016/0032-0633(81)90141-0

Dimmock, A. P., Hietala, H., & Zou, Y. (2020). Compiling magnetosheath statistical data sets under specific solar wind conditions: Lessons learnt from the dayside kinetic southward IMF GEM challenge. *Earth and Space Science*, *7*(6), e2020EA001095. https://doi.org/10.1029/2020EA001095

Eggington, J. W. B., Eastwood, J. P., Mejnertsen, L., Desai, R. T., & Chittenden, J. P. (2020). Dipole tilt effect on magnetopause reconnection and the steady-state magnetosphere-ionosphere system: Global MHD simulations. *Journal of Geophysical Research: Space Physics*, *125*(7), e2019JA027510. https://doi.org/10.1029/2019JA027510

Erkaev, N. V., Farrugia, C. J., & Biernat, H. K. (1998). Comparison of gasdynamics and MHD predictions for magnetosheath flow. In J. Moen, A. Egeland, & M. Lockwood (Eds.), *Polar cap boundary phenomena, NATO ASI series* (Vol. 509, pp. 27–40). Springer. https://doi.org/10.1007/978-94-011-5214-3_3

Erkaev, N. V., Mezentsev, A., & Biernat, H. (2006). Influence of the interplanetary magnetic field on the solar wind flow about planetary obstacles. *Space Science Reviews*, *122*(1–4), 209–219. https://doi.org/10.1007/s11214-006-6059-z

Fuselier, S. A., Petrinec, S. M., Reiff, P. H., Birn, J., Baker, D. N., Cohen, I. J., et al. (2024). Global-scale processes and effects of magnetic reconnection on the geospace environment. *Space Science Reviews*, *220*(4), 34. https://doi.org/10.1007/s11214-024-01067-0

Gershenfeld, N. (2003). *The nature of mathematical modeling*. Cambridge University Press.

Jelínek, K., Němeček, Z., & Šafránková, J. (2012). A new approach to magnetopause and bow shock modeling based on automated region identification. *Journal of Geophysical Research*, *117*(A5), A05208. https://doi.org/10.1029/2011JA017252.1

Jung, J., Connor, H., Dimmock, A., Sembay, S., Read, A., & Soucek, J. (2024). Mshpy23: A user-friendly, parameterized model of magnetosheath conditions. *Earth and Planetary Physics*, *8*(1), 89–104. https://doi.org/10.26464/epp2023065

Kobel, E., & Flückiger, E. O. (1994). A model of the steady state magnetic field in the magnetosheath. *Journal of Geophysical Research*, *99*(A12), 23617–23622. https://doi.org/10.1029/94JA01778

Lin, R. L., Zhang, X. X., Liu, S. Q., Wang, Y. L., & Gong, J. C. (2010). A three-dimensional asymmetric magnetopause model. *Journal of Geophysical Research*, *115*(A4), A04207. https://doi.org/10.1029/2009JA014235

Lu, J. Y., Zhou, Y., Ma, X., Wang, M., Kabin, K., & Yuan, H. Z. (2019). Earth's bow shock: A new three-dimensional asymmetric model with dipole tilt effects. *Journal of Geophysical Research: Space Physics*, *124*(7), 5396–5407. https://doi.org/10.1029/2018JA026144

Mead, G. D., & Fairfield, D. H. (1975). A quantitative magnetospheric model derived from spacecraft magnetometer data. *Journal of Geophysical Research*, *80*(4), 523–534. https://doi.org/10.1029/JA080i004p00523

Michotte de Welle, B., Aunai, N., Lavraud, B., Génot, V., Nguyen, G., Ghisalberti, A., et al. (2024). Global environmental constraints on magnetic reconnection at the magnetopause from in situ measurements. *Journal of Geophysical Research: Space Physics*, *129*(8), e2023JA032098. https://doi.org/10.1029/2023JA032098

Michotte de Welle, B., Aunai, N., Nguyen, G., Lavraud, B., Génot, V., Jeandet, A., & Smets, R. (2022). Global three-dimensional draping of magnetic field lines in Earth's magnetosheath from in-situ spacecraft measurements. *Journal of Geophysical Research: Space Physics*, *127*(12), e2022JA030996. https://doi.org/10.1029/2022JA030996

Narita, Y., Töpfer, S., & Schmid, D. (2023). Scalar-potential mapping of the steady-state magnetosheath model. *Annals of Geophysics*, *42*, 79–89. https://doi.org/10.5194/angeo-42-79-2024

Owen, C. J., Slavin, J. A., Richardson, I. G., Murphy, N., & Hynds, R. J. (1995). Average motion, structure and orientation of the distant magnetotail determined from remote sensing of the edge of the plasma sheet boundary layer with E > 35 keV ions. *Journal of Geophysical Research*, *100*(A1), 185–204. https://doi.org/10.1029/94ja02417

Phan, T.-D., Paschmann, G., Baumjohann, W., Sckopke, N., & Lühr, H. (1994). The magnetosheath region adjacent to the dayside magnetopause: AMPTE/IRM observations. *Journal of Geophysical Research*, *99*(1), 121–141. https://doi.org/10.1029/gm090p0115

Press, W. H., Teukolsky, S. A., Vetterling, W. T., & Flannery, B. P. (1992). *Numerical recipes* (2nd ed.). Cambridge University Press.

Pudovkin, M. I., Besser, B. P., Zaitseva, S. A., Lebedeva, V. V., & Meister, C.-V. (2001). Magnetic barrier in case of a southward interplanetary magnetic field. *Journal of Atmospheric and Solar-Terrestrial Physics*, *63*(10), 1075–1083. https://doi.org/10.1016/s1364-6826(01)00023-2

Pudovkin, M. I., & Semenov, V. S. (1985). Magnetic field reconnection theory and the solar wind - Magnetosphere interaction: A review. *Space Science Reviews*, *41*(1–2), 1–89. https://doi.org/10.1007/bf00241346

Russell, C. T. (1972). The configuration of the magnetosphere, in: *Critical problems of magnetospheric physics*, (Eds.). C. R. Dyer, *Inter-union committee on solar-terrestrial physics*, National Academy of Sciences,

Samsonov, A. (2006). Numerical modelling of the Earth's magnetosheath for different IMF orientations. *Advances in Space Research*, *38*(8), 1652–1656. https://doi.org/10.1016/j.asr.2005.06.009

Shue, J.-H., Chao, J. K., Fu, H. C., Russell, C. T., Song, P., Khurana, K. K., & Singer, H. J. (1997). A new functional form to study the solar wind control of the magnetopause size and shape. *Journal of Geophysical Research*, *102*(5), 9497–9511. https://doi.org/10.1029/97JA00196

Sibeck, D. G., Siscoe, G. L., Slavin, J. A., Smith, E. J., Tsurutani, B. T., & Lepping, R. P. (1985). The distant magnetotail's response to a strong interplanetary magnetic field By: Twisting, flattening, and field line bending. *Journal of Geophysical Research*, *90*(A5), 4011–4019. https://doi.org/10.1029/ja090ia05p04011

Siscoe, G. L., Crooker, N. U., Erickson, G. M., Sonnerup, B. U. Ö., Maynard, N. C., Schoendorf, J. A., et al. (2002). MHD properties of magnetosheath flow. *Planetary and Space Science*, *50*(issues 5–6), 461–471. https://doi.org/10.1016/S0032-0633(02)00026-0

Sotirelis, T., & Meng, C.-I. (1999). Magnetopause from pressure balance. *Journal of Geophysical Research*, *104*(4), 6889–6898. https://doi.org/10.1029/1998ja900119

Soucek, J., & Escoubet, C. P. (2012). Predictive model of magnetosheath plasma flow and its validation against CLuster and THEMIS data. *Annals of Geophysics*, *30*(6), 973–982. https://doi.org/10.5194/angeo-30-973-2012

Tsyganenko, N. A. (1990). Quantitative models of the magnetospheric magnetic field: Methods and results *Space Sci., Rev. Space Science Reviews*, *54*(1–2), 75–186. https://doi.org/10.1007/bf00168021

Tsyganenko, N. A., & Andreeva, V. A. (2015). A forecasting model of the magnetosphere driven by an optimal solar wind coupling function. *Journal of Geophysical Research: Space Physics*, *120*(10), 8401–8425. https://doi.org/10.1002/2015JA021641

Tsyganenko, N. A., Karlsson, S. B. P., Kokubun, S., Yamamoto, T., Lazarus, A. J., Ogilvie, K. W., et al. (1998). Global configuration of the magnetotail current sheet as derived from Geotail, Wind, IMP 8 and ISEE 1/2 data. *Journal of Geophysical Research*, *102*(A4), 6827–6841. https://doi.org/10.1029/97ja03621

Tsyganenko, N. A., & Russell, C. T. (1999). Magnetic signatures of the distant polar cusps: Observations by Polar and quantitative modeling. *Journal of Geophysical Research*, *104*(A11), 24–939. https://doi.org/10.1029/1999ja900279

Tsyganenko, N. A., Semenov, V. S., & Erkaev, N. V. (2023). Data-based modeling of the magnetosheath magnetic field. *Journal of Geophysical Research: Space Physics*, *128*(11), e2023JA031665. https://doi.org/10.1029/2023JA031665

Tsyganenko, N. A., Semenov, V. S., Erkaev, N. V., & Gubaidulin, N. T. (2024). Magnetic fields and electric currents around the dayside magnetopause as inferred from data-constrained modeling. *Front. Astron. Space Sci.*, *11*, 1425165. https://doi.org/10.3389/fspas.2024.1425165

Vokhmyanin, M. V., Stepanov, N. A., & Sergeev, V. A. (2019). On the evaluation of data quality in the OMNI interplanetary magnetic field database. *Space Weather*, *17*(3), 476–486. https://doi.org/10.1029/2018SW002113

Walsh, B. M., Sibeck, D. G., Wang, Y., & Fairfield, D. H. (2012). Dawn-dusk asymmetries in the Earth's magnetosheath. *Journal of Geophysical Research*, *117*(A12), A12211. https://doi.org/10.1029/2012JA018240

Wang, Y. L., Raeder, J., & Russell, C. T. (2004). Plasma depletion layer: Magnetosheath flow structure and forces. *Annals of Geophysics*, *22*(3), 1001–1017. https://doi.org/10.5194/angeo-22-1001-2004

Zhang, H., Fu, S., Pu, Z., Lu, J., Zhong, J., Zhu, C., et al. (2019). Statistics on the magnetosheath properties related to magnetopause magnetic reconnection. *The Astrophysical Journal*, *880*(2), 122. https://doi.org/10.3847/1538–4357/ab290e